


Unraveling femtosecond spin and charge dynamics with extreme ultraviolet transverse MOKE spectroscopy

Henrike Probst¹, Christina Möller¹, Maren Schumacher¹, Thomas Brede², John Kay Dewhurst³, Marcel Reutzel¹, Daniel Steil¹, Sangeeta Sharma³, G. S. Matthijs Jansen^{1,*} and Stefan Mathias^{1,†}

¹*1st Institute of Physics, University of Göttingen, Friedrich-Hund-Platz 1, 37077 Göttingen, Germany*

²*Institute of Materials Physics, University of Göttingen, Friedrich-Hund-Platz 1, 37077 Göttingen, Germany*

³*Max-Born-Institute for Non-linear Optics and Short Pulse Spectroscopy, Max-Born Strasse 2A, 12489 Berlin, Germany*

 (Received 5 June 2023; revised 15 October 2023; accepted 6 December 2023; published 26 January 2024)

The magneto-optical Kerr effect (MOKE) in the extreme ultraviolet (EUV) regime has helped to elucidate some of the key processes that lead to the manipulation of magnetism on ultrafast timescales. However, as we show in this paper, the recently introduced spectrally resolved analysis of such data can lead to surprising experimental observations, which might cause misinterpretations. Therefore, an extended analysis of the EUV magneto-optics is necessary. Via experimental determination of the dielectric tensor, we find here that the nonequilibrium excitation in an ultrafast magnetization experiment can cause a rotation of the off-diagonal element of the dielectric tensor in the complex plane. In direct consequence, the commonly analyzed magneto-optic asymmetry may show time-dependent behavior that is not directly connected to the magnetic properties of the sample. We showcase such critical observations for the case of ultrafast magnetization dynamics in Ni, and give guidelines for the future analysis of spectrally resolved magneto-optical data and its comparison with theory.

DOI: [10.1103/PhysRevResearch.6.013107](https://doi.org/10.1103/PhysRevResearch.6.013107)

I. INTRODUCTION

The discovery of subpicosecond quenching of the ferromagnetic order in laser-excited nickel has heralded a global research initiative on ultrafast magnetism [1], first with the aim to understand light-matter interaction in ferromagnetic matter and ultimately aiming to control the magnetic state by light on ultrashort timescales [2,3]. Owing to the exceptional time resolution enabled by femtosecond laser pulses, pump-probe spectroscopy based on the magneto-optical Kerr or Faraday effect is the method of choice for many studies on ultrafast magnetization dynamics. However, a challenging aspect of such studies is the commonly rather weak strength of the magneto-optical effect in combination with the presence of significant changes in the electronic (i.e., nonmagnetic) structure of the material. The validation of the magneto-optical spectroscopy method of choice and the exclusion of nonmagnetic artifacts has therefore always been a high priority. Such studies were performed for the first near-infrared magneto-optical Kerr effect (MOKE) experiments [4–8], and have been performed for many of the newly developed mag-

netic spectroscopy techniques ranging from the terahertz to the x-ray region that now exist [9–11].

Extreme ultraviolet (EUV) or x-ray radiation is particularly promising as a probe of the magnetic state, as access to the element-specific M and L edges enables elemental resolution in addition to excellent time resolution. Using various techniques such as the transverse magneto-optical Kerr effect (T-MOKE), the resonant Faraday effect, x-ray magnetic circular dichroism (XMCD), or x-ray resonant magnetic reflectivity [12–16], EUV and x-ray-based studies have helped to verify and elucidate a number of key findings in ultrafast magnetism in the last 15 years [14,17–27]. Recently, the capabilities of EUV and x-ray magneto-optical spectroscopy have dramatically increased; for one, due to the developments at large-scale free-electron facilities, and for another, due to the development of ever more powerful laser-driven EUV spectroscopy facilities [28–32]. This has improved the spectral resolution and data quality to such an extent that the individual absorption edges can now be analyzed in a completely energy-resolved manner. Such spectrally resolved analysis has allowed a valuable insight into the light-driven dynamics, and has for example led to the verification of the so-called optical intersite spin-transfer (OISTR) effect [21–23,33,34].

However, especially on the few-femtosecond timescale where the femtosecond pump pulse drives the electron and spin systems into a nonthermal, out-of-equilibrium state, strong energy-dependent modifications of the refractive index can be expected and extra care must be taken to exclude nonmagnetic artifacts. Particularly in the context of EUV T-MOKE, it has already been recognized that the interpretation of such data asks for a more detailed analysis of the collected

*gsmjansen@uni-goettingen.de

†smathias@uni-goettingen.de

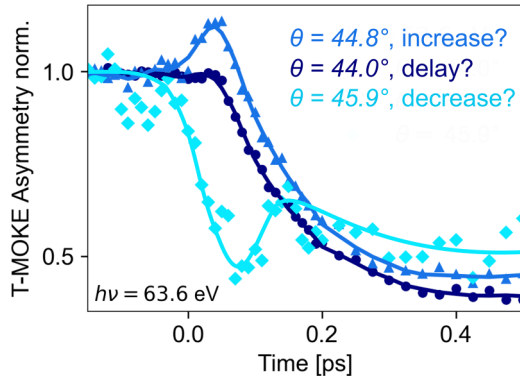


FIG. 1. Increase, delay, or decrease of the spin dynamics? Very different dynamics in the T-MOKE asymmetry are observed at 63.6 eV ($\pm 2\%$) photon energy for slightly different angles of incidence (dark blue, 44° ; blue, 44.8° ; light blue, 45.9°). The measurement clearly illustrates that a direct interpretation of T-MOKE asymmetry with ultrafast magnetization dynamics can be highly problematic. Note that the solid lines serve as a guide to the eye.

T-MOKE data [10,21,35,36]. Similarly, the comparison of magneto-optical spectroscopy data with state-of-the-art time-dependent density functional theory (TDDFT) and similar theoretical methods requires careful analysis [37,38].

The urgency for a sophisticated analysis of spectrally resolved T-MOKE data can be best introduced with an exemplary measurement of ultrafast magnetization dynamics in the prototypical $3d$ ferromagnet Ni. Figure 1 shows transient T-MOKE asymmetry data, measured with our setup [31], and analyzed at 63.6 eV ($\pm 2\%$) EUV photon energy for slightly varying incidence angles. Very disturbingly, the transient dynamics of the T-MOKE asymmetry shows completely distinct behavior. In particular, for the very same ultrafast pump-probe experiment, all heavily discussed experimental signatures, i.e., an increase, a delay, and a decrease in the T-MOKE asymmetry, can be identified, which have previously been used to identify the OISTR effect [21–23], the influence of exchange scattering [17], and the typical demagnetization process [13]. Having just the information of this particular measurement available, all previous interpretations of T-MOKE data would be in question. In the following, we will show how such critical T-MOKE data need to be analyzed to obtain reliable access to the true spin dynamics.

The overall topic of the paper is illustrated in Fig. 2. Usually, the main quantity of interest is the global magnetization (top right) or the energy-resolved magnetic moment, given by the difference in majority and minority spins in the density of states (DOS) (bottom right). In EUV T-MOKE experiments, the aim is to probe the time-dependent magnetization and magnetic moment; however, neither magnetization (orange arrow) nor the energy-resolved magnetic moment (red arrow) is directly measured. Rather, as an optical technique, T-MOKE probes the dielectric tensor and is specifically sensitive to the off-axis dielectric tensor element ϵ_{xy} [39]. Since the dielectric tensor (including ϵ_{xy}) can be calculated from TDDFT calculations of the spin-resolved density of states [37,38,40–42], a time-resolved extraction of ϵ_{xy} from T-MOKE data would allow for a quantitative comparison of experimental T-MOKE data and theoretical calculations.

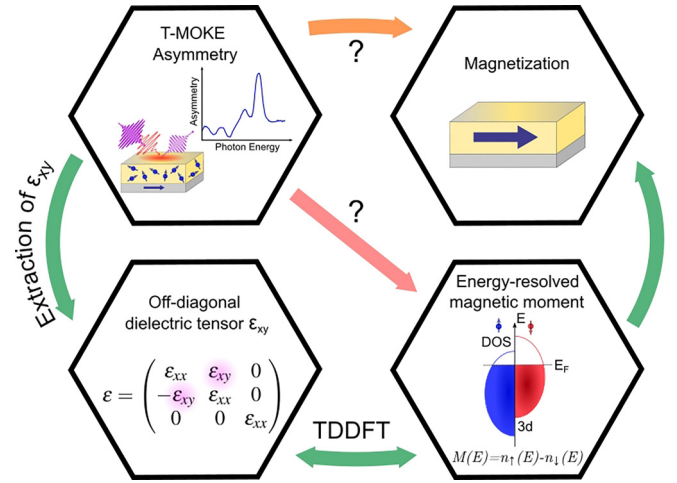


FIG. 2. Overview of the connections between experimental magneto-optical signal, the off-diagonal tensor-element, and the magnetization.

In our work, we therefore develop a robust and easy-to-implement method to analyze transient dynamics of the dielectric tensor. With the help of this analysis, we elucidate that the nonequilibrium excitation by the optical pulse can lead to a rotation of the off-diagonal element of the dielectric tensor in the complex plane. This rotational behavior can lead to the observed increase, delay, and decrease of the T-MOKE asymmetry as seen in Fig. 1, and these differing signals simply depend on the used measurement geometry of the T-MOKE experiment, i.e., the angle of incidence of the EUV light. As TDDFT is also able to provide transient dynamics of the dielectric tensor, we find that a direct comparison of experiment and theory becomes possible via such a dielectric tensor analysis from the data. In Ni, via comparison with theory, we can show that the observed dynamics at early times of the pump excitation (< 50 fs) is dominantly driven by spin-conserving transitions in the minority channel. Besides a comparison of the same quantity, our approach also ensures that spectral broadening, multiple edges, and overlapping edges from multiple elements in multicomponent materials are properly taken into account.

II. MAGNETO-OPTICAL SPECTROSCOPY

A. Magneto-optical asymmetry in T-MOKE

Previous magneto-optical studies have attempted to make a direct connection between the magneto-optical signal and the element-specific magnetization properties of the sample after an ultrafast excitation. However, as shown above and discussed in Fig. 2, the relation between the measurement signal in a T-MOKE experiment and the magnetization is more complex, even in the equilibrium case. At the microscopic scale, the interaction of light with a material is given by the complex-valued dielectric tensor ϵ , which can be derived by counting the number of allowed optical transitions within the spin-resolved band structure [38,43–46]. For a magnetic material, the imbalance between the different spin channels leads to off-diagonal terms in the dielectric tensor, which couple light fields of orthogonal polarization. For a typical

(cubic) magnetic material that is magnetized along the z axis, the dielectric tensor is commonly expressed as

$$\varepsilon = \begin{pmatrix} \varepsilon_{xx} & \varepsilon_{xy} & 0 \\ -\varepsilon_{xy} & \varepsilon_{xx} & 0 \\ 0 & 0 & \varepsilon_{zz} \end{pmatrix}. \quad (1)$$

Here, ε_{xx} can be directly related to the nonmagnetic refractive index, mostly written as

$$\sqrt{\varepsilon_{xx}} = n = 1 - \delta + i\beta, \quad (2)$$

while the off-axis dielectric tensor element ε_{xy} describes the magneto-optical response of the material.

Through the Fresnel equations, it is possible to express the signal in various magneto-optical techniques in terms of the dielectric tensor components. For example, for XMCD, it is known that a signal can be extracted that is proportional to $\text{Re}(\varepsilon_{xy})$ [37,38]. For T-MOKE, the reflectivity of a single vacuum/magnetic material interface can to good accuracy be expressed as [47]

$$R_{\uparrow/\downarrow} = |R_0|^2 + |R_m \varepsilon_{xy}|^2 \pm \text{Re}\{2R_0^* R_m \varepsilon_{xy}\}, \quad (3)$$

where $R_0 = \frac{n \cos \theta_i - \cos \theta_t}{n \cos \theta_i + \cos \theta_t}$ and $R_m = \frac{\sin 2\theta_i}{n^2 (n \cos \theta_i + \cos \theta_t)}$ are the (complex-valued) nonmagnetic and magnetic contributions to the reflectivity, respectively. $\text{Re}\{\cdot\}$ indicates the real part, and the incidence angle θ_i and refraction angle θ_t are related by Snell's law. The \pm sign in Eq. (3) is directly linked to the magnetization direction, where switching the magnetization direction also switches the sign.

Based on Eq. (3), the commonly used measurement strategy in EUV T-MOKE is to measure the reflected intensity $I_{\uparrow/\downarrow}$ (which is proportional to $R_{\uparrow/\downarrow}$), and subsequently calculate the T-MOKE asymmetry for bulk magnetic material by [10,35,38,48]

$$A = \frac{I_{\uparrow} - I_{\downarrow}}{I_{\uparrow} + I_{\downarrow}} = \frac{2\text{Re}(R_0^* R_m \varepsilon_{xy})}{|R_0|^2 + |R_m \varepsilon_{xy}|^2}. \quad (4)$$

By alternately measuring I_{\uparrow} and I_{\downarrow} , this allows to efficiently filter out variations in the light source intensity. Then, it is useful to consider the following assumptions: if $|R_m \varepsilon_{xy}|^2 \ll |R_0|^2$ and the refractive index n is constant, then the transient asymmetry $A(t)$ can be normalized to a reference asymmetry A_{ref} (commonly the T-MOKE asymmetry of the sample in equilibrium), and the signal

$$\frac{A(t)}{A_{\text{ref}}} = \frac{\text{Re}(R_0^* R_m \varepsilon_{xy}(t))}{\text{Re}(R_0^* R_m \varepsilon_{xy}^{\text{ref}})} \quad (5)$$

is acquired. Now, a further assumption can be made to finally quantitatively link the observed signal $A(t)$ to a change in ε_{xy} : namely, that the angle of ε_{xy} in the complex plane does not change and only the magnitude $|\varepsilon_{xy}|$ decreases or increases. However, as will become clear in the following analysis, the data that are presented in Fig. 1 unambiguously show that this set of assumptions cannot hold.

B. Angle dependence of the T-MOKE asymmetry

It is well known that the reflectivity of a sample, and more specifically also the T-MOKE signal, depends strongly on the angle of incidence, θ_i [17,24,49]. This is particularly

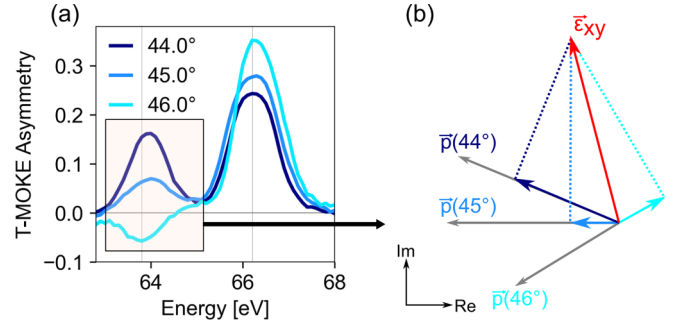


FIG. 3. Angle dependence of the static T-MOKE asymmetry for Ni. (a) The observed T-MOKE asymmetry for the 22-nm Ni sample for three different incidence angles θ_i close to 45° . (b) Schematic representation of the probe vectors following Eq. (6) for the different incidence angles in (a), and the ε_{xy} that was determined from these measurements. For the calculation, we used the same sample composition and refractive index values as in Sec. III A.

true for the magneto-optical reflectivity close to the Brewster angle, where a strong magneto-optical signal is observed as the nonmagnetic reflection is strongly suppressed. In order to understand this behavior, it is useful to consider $\varepsilon_{xy} = \text{Re}(\varepsilon_{xy}) + i \text{Im}(\varepsilon_{xy})$ as a vector in the complex plane: $\vec{\varepsilon}_{xy}$. Approximating the T-MOKE asymmetry to depend linearly on ε_{xy} [i.e., using $|R_0|^2 \gg |R_m \varepsilon_{xy}|^2$ in Eq. (4)], we rewrite Eq. (4) as

$$\begin{aligned} A(\varepsilon_{xy}) &\approx \frac{2}{|R_0|^2} \text{Re}(R_0^* R_m \varepsilon_{xy}) \\ &= \frac{2}{|R_0|^2} [\text{Re}(R_0 R_m^*) \text{Re}(\varepsilon_{xy}) + \text{Im}(R_0 R_m^*) \text{Im}(\varepsilon_{xy})] \\ &= \vec{p}_\theta \cdot \vec{\varepsilon}_{xy} = |\vec{p}_\theta| |\vec{\varepsilon}_{xy}| \cos(\angle(\vec{p}_\theta, \vec{\varepsilon}_{xy})). \end{aligned}$$

This analysis shows that it is possible to interpret the T-MOKE asymmetry $A(\vec{\varepsilon}_{xy})$ as the inner product of $\vec{\varepsilon}_{xy}$ with a *probe vector* \vec{p}_θ . For the simple case of a single vacuum/magnet interface, \vec{p}_θ is (up to a scaling factor) proportional to $(\text{Re}(R_0 R_m^*), \text{Im}(R_0 R_m^*))$. More generally, we define the probe vector as the derivative of the T-MOKE asymmetry with respect to ε_{xy} :

$$\vec{p}_\theta = \left(\frac{\partial A}{\partial \text{Re}(\varepsilon_{xy})}, \frac{\partial A}{\partial \text{Im}(\varepsilon_{xy})} \right). \quad (6)$$

We note that since \vec{p}_θ depends only on the geometric and nonmagnetic properties of the sample, it can be calculated without (precise) *a priori* knowledge of ε_{xy} . It is most important, however, to realize that \vec{p}_θ rotates strongly in the complex plane as the angle of incidence θ_i of the EUV light in the T-MOKE measurement changes.

This strong θ_i angle of incidence dependence is critical, because the T-MOKE asymmetry is proportional to the inner product of the vectors $\vec{\varepsilon}_{xy}$ and the probe vector \vec{p}_θ . If the angle $\angle(\vec{p}_\theta, \vec{\varepsilon}_{xy})$ between these vectors approaches 90° , a particularly strong dependence of the asymmetry on the geometrical factors must be expected. This situation is illustrated in Fig. 3(a), where the measured T-MOKE asymmetry for three incidence angles close to $\theta_i = 45^\circ$ is shown. In the spectral region marked with a rectangle, the T-MOKE

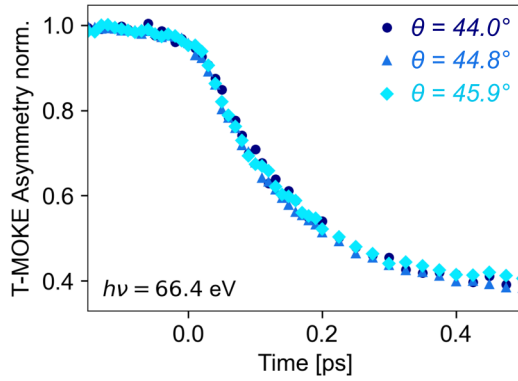


FIG. 4. Transient magneto-optical asymmetry at 66.4 eV, i.e., at the Ni resonance, yields identical dynamics for each angle.

asymmetry is strongly angle of incidence dependent, and even flips from positive to negative values. This can be understood by looking at the schematic in Fig. 3(b), which illustrates the positive-to-negative change of the inner product of \vec{p}_θ and $\vec{\epsilon}_{xy}$ as a function of the angle of incidence and therewith $\langle \vec{p}_\theta, \vec{\epsilon}_{xy} \rangle$.

Another very important aspect for angles $\langle \vec{p}_\theta, \vec{\epsilon}_{xy} \rangle \approx 90^\circ$ is the realization that even small rotations of ϵ_{xy} in time-resolved measurements would lead to sign changes in the measured T-MOKE asymmetry. Indeed, we will show that this is exactly the reason for the disturbing data presented in Fig. 1, which were analyzed at a photon energy of 63.6 eV: here, a small transient rotation of ϵ_{xy} leads to very different transient T-MOKE asymmetries for different angles of incidence, as we will fully analyze below.

On the other hand, if $\langle \vec{p}_\theta, \vec{\epsilon}_{xy} \rangle$ is much larger or smaller than 90° , as is the case in the spectral region around 66 eV, no such peculiar behavior is expected. An analysis of transient T-MOKE asymmetry around 66 eV for different angles of incidence consequently yields perfectly identical results (Fig. 4), and the transient T-MOKE asymmetry now reliably reflects the ultrafast magnetic behavior.

In summary, we can already conclude that angles of $\langle \vec{p}_\theta, \vec{\epsilon}_{xy} \rangle \approx 90^\circ$ can lead to results in the time-resolved data that are not straightforward to interpret. However, this particular situation can readily be identified, if the asymmetry in a certain spectral range is highly sensitive to the EUV angle of incidence and flips sign or approaches zero.

C. Beyond the bulk approximation

In the previous analysis, we have focused specifically on a single vacuum/magnet interface, as the Fresnel equations for such a case are comparatively simple. However, the magnetic samples studied in ultrafast magnetism, including also this study, are often best described as multilayer structures. In particular, a capping layer is often included to protect the magnetic material from the oxidizing environment; and if no capping layer is included, commonly a native oxide layer forms. For such a sample, expressions for the magnetization-dependent reflectivity can be derived using the transfer matrix formalism [50–52]. In the present study, we have implemented the transfer matrix formalism from Ref. [51] using a symbolic

math package (SymPy) [53] for PYTHON to calculate the reflectivity, the T-MOKE asymmetry, and the probe vectors \vec{p}_θ without relying on assumptions concerning the strength of the magneto-optic response.

III. DETERMINATION OF DIELECTRIC TENSOR FROM T-MOKE DATA

The strong angle dependence of the T-MOKE asymmetry can be leveraged in order to extract the complex-valued off-diagonal dielectric tensor element ϵ_{xy} [47,49,54]. Here, we present a unique approach to such magneto-optical reflectometry where only a small range of incidence angles needs to be measured for complete access to ϵ_{xy} at the given photon energies. Specifically, this approach takes advantage of the strong enhancement and dependence on the incidence angle of the T-MOKE asymmetry around 45° , and furthermore makes use of the well-known nonmagnetic components of the dielectric tensor, which allows us to reliably calculate the probe vectors. This approach provides two crucial advantages: the experimental setup can be integrated into a typical EUV T-MOKE setup without requiring a major overhaul, and since only a small number of incidence angles need to be measured, full femtosecond time-resolved magneto-optical spectroscopy is possible with only a small (less than fivefold) increase in the measurement time.

In the following, we will first discuss the extraction of the static off-diagonal dielectric tensor element, which is necessary in order to calibrate certain experimental parameters, before we continue with the extraction of the time-resolved dielectric tensor.

A. Extraction of the static off-diagonal dielectric tensor element

Several approaches exist to extract the magneto-optical dielectric tensor element ϵ_{xy} at extreme ultraviolet wavelengths [37,47,49,54,55]. For thin samples that are best probed in reflection, incidence-angle-dependent or polarization-dependent reflectivity measurements have demonstrated their value [47,49,54,56,57]. As these techniques rely on reflectivity measurements for linearly polarized light, they are commonly implemented in laboratory-scale experiments based on high-order-harmonic generation. A limiting factor for the implementation of these techniques, however, is that they typically require a dedicated experimental geometry. Consequently, there is a need for an ϵ_{xy} measurement technique that is compatible with, and can be implemented in, currently existing EUV femtomagnetism experiments. Here, we present a magneto-optical reflectometry method (in the $\theta - 2\theta$ geometry) that we implemented in our tabletop femtosecond EUV T-MOKE spectroscopy setup [31]. This was made possible by the implementation of a motorized, nonmagnetic and UHV-compatible tip-tilt sample holder (SmarAct GmbH), which enabled a scan range of $>2^\circ$ (see Fig. 10 in Appendix A). As such, we anticipate that the method can be rapidly implemented in many setups that are currently being used for fixed-angle EUV T-MOKE.

In order to gain access to the off-axis dielectric tensor element of a magnetized Ni thin film, we performed a series of T-MOKE asymmetry measurements at 11 different incidence

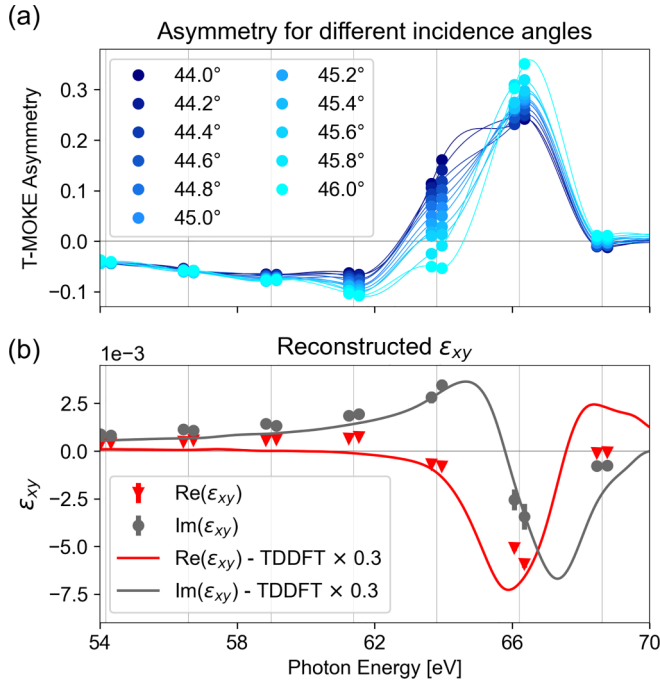


FIG. 5. Determination of a static ϵ_{xy} . (a) T-MOKE asymmetry for 11 incidence angles close to 45° . Due to the high spectral resolution, we were able to evaluate the T-MOKE asymmetry at two energies for each high-order harmonic, indicated by points. The connecting lines serve as a guide to the eye for the T-MOKE asymmetry. (b) For comparison, we have calculated the real and imaginary parts of ϵ_{xy} by TDDFT. We find a good agreement with regard to the photon energy dependence, although TDDFT predicts an overall stronger magneto-optical response. The standard deviation of the reconstructed ϵ_{xy} is shown by error bars, although we note that the error margin is generally so small that the error bar falls within the marker size. For a discussion of the systematic errors see Sec. III B.

angles [shown in Fig. 5(a)]. The sample consists of a 22-nm Ni film that was deposited by sputtering on a Si_3N_4 -coated Si wafer. This thickness was chosen such that femtosecond optical pulses will excite the sample homogeneously (see Fig. 11 in Appendix A), while simultaneously being thick enough that the reflection at the Ni/ Si_3N_4 interface does not modify the observed T-MOKE asymmetry strongly. The 112-nm Si_3N_4 layer is thick enough that no reflection from the Si_3N_4 /Si interface has to be accounted for. Finally, the Ni layer possesses a thin, native Ni oxide layer on top, which reduces the strength of the T-MOKE asymmetry. From an x-ray reflectivity measurement, we determined the NiO layer to be approximately 2 nm thick (see Appendix A for full details of the x-ray reflectivity analysis). In our analysis, we then use the transfer matrix formalism and calculate expressions for the full three-layer system, including the 2-nm NiO capping layer, the 22-nm Ni magnetic layer, and the 112-nm Si_3N_4 bottom layer. Following earlier work where it was found that the subnanometer interface roughness does not strongly affect the EUV T-MOKE signal [24], we have not included interface roughness in the model.

For our sample, the T-MOKE asymmetry depends on the complex-valued refractive indices of Ni, NiO, and Si_3N_4 , the layer thicknesses, the incidence angle, and the

complex-valued ϵ_{xy} of Ni. Using the result of the transfer matrix formalism as the model for the sample, the energy-resolved complex-valued ϵ_{xy} can be determined from a set of angle-dependent T-MOKE asymmetry measurements using a standard least-squares fitting procedure. In order to facilitate a reliable determination of ϵ_{xy} with few measurements over a small angular range, we fit only the value of ϵ_{xy} and fix the other parameters, including the complex-valued refractive indices, to known (literature) values. We retrieve the values for the dispersive (real) part of the refractive index δ from Ref. [58], while we used more recent measurements from Ref. [37] for the absorptive (imaginary) part β . Using other sources for β such as Ref. [55] or [58] leads to small variations in the overall amplitude of ϵ_{xy} , but does not affect the photon-energy dependence significantly.

The best-fit values for the real and imaginary parts of the off-diagonal tensor element ϵ_{xy} in Ni are shown in Fig. 5(b). As expected, the largest values can be found around the M absorption edges of Ni around 66 eV (M_3 edge). We also find a good qualitative agreement with previously published data [37,55]. Furthermore, the dielectric tensor can be accurately calculated based on (time-dependent) density functional theory complemented by calculations in the GW framework to achieve an accurate description of the $3p$ core states [37,38,46,59]. Here, we find a good agreement between experiment and theory on the shape of the dielectric tensor, although theory indicates an overall larger amplitude of ϵ_{xy} . We attribute the discrepancy in the amplitude to a common overestimation of the film-averaged magnetic moment in the TDDFT calculation [35,60]. In this regard, a better match between experiment and theory, particularly for the spectral region just above the edge, was recently also achieved by manually reducing the exchange splitting [37].

B. Systematics and uncertainties

There are several experimental uncertainties that may influence the extracted values for ϵ_{xy} . These include statistical and systematic effects. The statistical effects include shot-to-shot intensity fluctuations, position-dependent detection efficiency on the camera, and an uncertainty in the relative angle determination. As we performed a large number of angle-dependent measurements with a relatively long measurement time, however, we estimate that the statistical errors are negligible compared to the systematic ones. We have identified several possible sources of systematic errors, which we analyze in the context of the present Ni sample.

First, the leading source of systematic errors is the calibration of the incidence angle. From Fig. 3, it is clear that a change in the incidence angle leads to a rotation of the probe vectors, as well as a change in the length. Therefore, a systematic error in the angle determination leads to a rotation of $\vec{\epsilon}_{xy}$ in the complex plane, as well as a change in amplitude. Performing the full ϵ_{xy} reconstruction for different angle calibrations, we find that a 0.5° calibration error in the incidence angle typically leads to a rotation of $\vec{\epsilon}_{xy}$ by 10° and a scaling of the amplitude by 10%. Considering the experimental setup, we estimate that the absolute angle calibration is accurate to within 0.3° .

Second, quantitative determination of the T-MOKE asymmetry relies on an accurate subtraction of the background signal in the spectrometer. This is particularly critical when the detected EUV flux is low. To avoid errors due to this effect, we have chosen to evaluate the data only at photon energies around the peaks of the high-order harmonic generation (HHG) spectrum. Nevertheless, we note that close to the HHG cutoff energy (≈ 70 eV, cf. Fig. 12 in Appendix A), the flux of each harmonic significantly decreases. At these photon energies, an imperfect background correction can lead to a reduction of the observed T-MOKE asymmetry and thereby an underestimation of the amplitude of ε_{xy} . For the data reported in this paper, we estimate this effect to be negligible.

Third, it was already discussed that the NiO capping influences the observed T-MOKE asymmetry. Unfortunately, no direct determination of the capping layer thickness was possible. Therefore, we have analyzed the influence of the capping layer thickness on the retrieved ε_{xy} values. Within the range of expected NiO thicknesses (1.5–2.5 nm), we find that a thicker (thinner) NiO capping would reduce (increase) the size of the observed T-MOKE asymmetry and therefore would lead to a slightly larger (smaller) amplitude of ε_{xy} . Here, 0.5 nm change corresponds to less than 10% change in the amplitude. Also, a comparatively small rotation of the extracted ε_{xy} can be observed. Overall, the effect due to uncertainty in the capping layer thickness is less pronounced than the effect due to the angle-of-incidence calibration.

Fourth, we note that the presented ε_{xy} reconstruction technique depends on accurate values for the nonmagnetic refractive indices of all materials in the sample. However, by performing the full analysis for different values of the refractive index of Ni (from Refs. [37,55,58]), we find only a minor effect on the shape and strength of ε_{xy} . Related to that, also an accurate calibration of the photon energy is necessary. Within the experimental uncertainty of the photon energy calibration, which is $<2\%$, we find no significant change in the reconstructed ε_{xy} .

C. Probing the transient dielectric tensor

Next, we proceed to determine the time-resolved ε_{xy} during optically induced ultrafast demagnetization with sufficient time resolution to trace the full demagnetization process and thereby provide an ideal basis for comparison with theoretical methods that describe the dynamics of the electron, spin, and lattice degrees of freedom. Compared to the static case that was previously discussed, we make two observations: First, as a consequence of the optical excitation, it is not possible to fix the refractive index to literature values; rather, the dynamical behavior of β and δ [see Eq. (2)] must be extracted from the experimental data. Second, the number of measured angles must be limited as much as possible to facilitate the measurement of a larger number of pump-probe delays. We find that these points can be addressed by choosing the reflectivity $R_{\uparrow/\downarrow}$ [Eq. (3); more precisely its equivalent from the transfer matrix formalism] as a starting point for the time-resolved analysis, rather than the T-MOKE asymmetry [Eq. (4)]. Instead of a single value per photon energy and pump-probe delay, this yields two measurement values (for two magnetization directions) which contain both magnetic and nonmagnetic contributions.

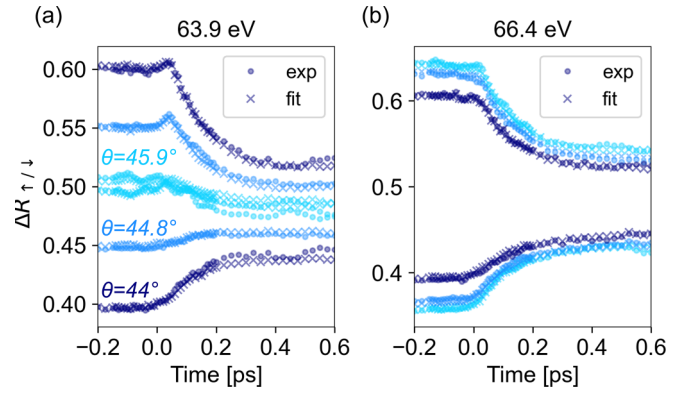


FIG. 6. Fit of the time-resolved data to extract both ε_{xy} and β . [(a), (b)] The measured (circles) and reconstructed (crosses) transient relative reflectivity $\Delta R_{\uparrow/\downarrow}(t)$ for opposite magnetization directions [cf. Eq. (7)] during optically induced magnetization dynamics for photon energies (a) just below and (b) close to the Ni M edge. Note that the fitting analysis considers each time step fully independently.

As the absolute reflectivity cannot be measured in our experiment, we consider only the relative changes compared to the unpumped ($t < 0$) case. From a measurement series of the delay-dependent intensity $I_{\uparrow/\downarrow}(t)$, we extract the relative reflectivity

$$\Delta R_{\uparrow/\downarrow}(t) = \frac{1}{2} \frac{R_{\uparrow/\downarrow}(t)}{R_{\uparrow/\downarrow}(t_{\text{ref}})} = \frac{I_{\uparrow/\downarrow}(t)}{I_{\uparrow}(t_{\text{ref}}) + I_{\downarrow}(t_{\text{ref}})}, \quad (7)$$

where t_{ref} indicates the reference time interval where the probe arrives at the sample before the pump pulse. This yields a signal that reflects the static asymmetry at times before the pump pulse and provides a measure of the transient magneto-optical and nonmagnetic reflectivity changes at times after the pump pulse has arrived. Figures 6(a) and 6(b) show such measurement data for the same experimental situation that was presented in Fig. 1, namely, the optically induced demagnetization of Ni.

The full data set contains the magnetization-dependent relative reflectivity for the full high-order harmonic spectrum at three incidence angles θ_i (44° , 44.8° , and 45.9° , as determined from the static analysis). In order to extract the time-dependent ε_{xy} , we apply a similar fitting procedure as was used in the static case: Each photon energy and each pump-probe delay are considered independently. For each combination of these, our reconstruction algorithm determines the optimal values for $\text{Re}(\varepsilon_{xy})$, $\text{Im}(\varepsilon_{xy})$, β , and δ .

We find that δ generally does not influence the predicted reflectivity strongly, and consequently it cannot accurately be determined with a least-squares fitting routine. To address this, we employ a self-consistent two-step approach:

- (1) Keeping δ fixed, we use a least-squares fitting to determine $\text{Re}(\varepsilon_{xy})$, $\text{Im}(\varepsilon_{xy})$, and β .
- (2) We use a Kramers-Kronig (KK) transform to determine δ [61].

Repeating steps 1 and 2 up to ten times has shown excellent convergence and a good reconstruction of the measured values, as shown in Figs. 6(a) and 6(b). We note that although $\text{Re}(\varepsilon_{xy})$ and $\text{Im}(\varepsilon_{xy})$ are also connected by the KK relations, the implementation of such a transform is challenging due

to the sparsely sampled nature of our spectrum. We have therefore achieved better results without linking $\text{Re}(\epsilon_{xy})$ and $\text{Im}(\epsilon_{xy})$ by KK. Consequently, for each combination of photon energy and pump-probe delay, we extract three independent variables ($\text{Re}(\epsilon_{xy})$, $\text{Im}(\epsilon_{xy})$, and β) from six independent measurements (two per angle of incidence).

D. Systematics and uncertainties in the time-resolved analysis

As the time-resolved ϵ_{xy} analysis directly builds upon our static measurement of ϵ_{xy} , most potential systematic errors carry over from the static to the dynamic analysis. For example, the angle-of-incidence calibration is matched to the static measurement, which can easily be done by comparing the shape of the before-excitation T-MOKE asymmetry. However, as these effects affect each time step identically, and we are mostly interested in relative dynamics, the impact of systematic errors in the static analysis is somewhat reduced. In order to verify this, we performed full time-resolved ϵ_{xy} analysis for several thicknesses of the NiO capping layer, namely, 1.5, 2.0, and 2.5 nm. These values all fall within the confidence interval of our x-ray reflectivity measurement; however, they lead to quantitative differences in the reconstructed ϵ_{xy} , as discussed in Sec. III B. Nevertheless, from the full time-resolved analysis for each of these assumed thicknesses, we find that we recover qualitatively the same result: at 64 eV, we observe a transient enhancement of $\text{Re}(\epsilon_{xy})$, while $\text{Re}(\epsilon_{xy})$ at 66 eV shows a monotonic decay (cf. Fig. 15 in Appendix A). For each thickness, we therefore find a qualitative agreement with the prediction from TDDFT, although the amplitude of the enhancement from experiment is a bit too small for 1.5-nm NiO, and too large for 2.5-nm NiO. This difference in amplitude is mostly caused by a change of the static reconstructed ϵ_{xy} [which determines the scale for the relative enhancement of $\text{Re}(\epsilon_{xy})$]. As was discussed in Sec. III B, the calibration of the incidence angle has a similar effect to the capping layer thickness, and this similarity also holds for the reconstructed ϵ_{xy} dynamics.

Beyond the systematic errors in the static ϵ_{xy} determination, the most important sources of uncertainty in the time-resolved analysis relate to the modeling of the dynamics. For example, it is known that superdiffusive spin currents may lead to depth-dependent spin dynamics [62], and this can affect the angle-resolved T-MOKE spectroscopy data [24,57]. An unconstrained depth-resolved analysis is not possible in this case, however, as time- and angle-resolved data are only available for three unique incidence angles over a small range. Therefore, we approximate the demagnetization process to be homogeneous over the full depth profile. This choice is supported by the sample composition, as no spin currents can flow into the insulating substrate. By performing data simulation and reconstruction for several smoothly varying depth-dependent magnetization profiles, we find that the time-resolved ϵ_{xy} analysis is always close to the sample-averaged dielectric tensor, and does not qualitatively change our result.

Depending on the exact composition of the sample under study, it is also necessary to account for optically induced changes in the capping layer. For the present sample, NiO/Ni/Si₃N₄, it is clear that changes in the NiO capping layer can change the refractive index at the Ni *M* edge,

which directly coincides with the measured magneto-optical spectroscopy signal. Refractive index changes in the capping layer could potentially modify the observed ϵ_{xy} dynamics. At present, the experimental data at three incidence angles are not enough to consider the dynamics in the NiO layer independently from the Ni layer. Instead, considering that the refractive index change on the femtosecond timescale is driven by hot electrons, we approximate the refractive index change in NiO to be proportional to the refractive index change in Ni itself. By varying the proportionality constant in the range from 0 to 2, we find that dynamics in the capping layer have only a small effect on the reconstructed ϵ_{xy} , which can be attributed to the thin capping layer thickness.

IV. INTERPRETATION

A. Rotation of ϵ_{xy}

Having reconstructed the transient dielectric tensor including both the magnetic (ϵ_{xy}) and nonmagnetic (ϵ_{xx}) parts, we proceed with the interpretation of these results. In a first step, it is instructive to return to the special case that was identified in Ni at 64 eV photon energy (Fig. 1). Figures 7(a) and 7(b) show the real and imaginary parts of the off-diagonal dielectric tensor element, respectively, as a function of time for two selected energies (more data, including the extracted variation of δ , are shown in Fig. 15 in the Appendix A). First, we recognize that the overall magnitude $|\epsilon_{xy}|$ decreases over time to approximately 40% of its original length after 600 fs. More interesting, however, we also see that $\text{Re}(\epsilon_{xy})$ and $\text{Im}(\epsilon_{xy})$ do not quench identically as a function of time, especially for $h\nu = 64$ eV, where a transient increase of $\text{Re}(\epsilon_{xy})$ is observed. This means that ϵ_{xy} must transiently rotate in the complex plane. This rotation in the complex plane is visualized in Fig. 8(a) and is a key factor in the explanation of the diverse transient effects that were observed in Ni at 64 eV (Fig. 1). However, we note that a rotation of ϵ_{xy} can also be observed for many other photon energies, and does not necessarily have a large impact on the T-MOKE asymmetry data, as is evident from the measurement shown in Fig. 4. Therefore, a rotation of ϵ_{xy} alone is not sufficient to explain the peculiar data of Fig. 1.

At 64 eV, we find that, in addition to the transient rotation of ϵ_{xy} , the probe vector \vec{p}_θ and the off-diagonal dielectric tensor element ϵ_{xy} are close to orthogonal. This is evident by the zero crossing of the static magnetic asymmetry for different angles of incidence (see Figs. 3 and 5). This situation does not occur at the other photon energies that we have observed, and it provides the second key to the explanation of the data in Fig. 1. The T-MOKE asymmetry can be approximated by the projection of ϵ_{xy} on the probe vectors \vec{p}_θ . In Fig. 8(b), we now apply this method again to visualize how the experimentally determined transient rotation of ϵ_{xy} can influence the measured T-MOKE asymmetry. We find that changes of the orientation of ϵ_{xy} can lead to dramatic effects, which furthermore depend strongly on the precise angle $\angle(\vec{p}, \vec{\epsilon}_{xy})$, and in particular whether this angle is more or less than 90°. We can readily construct scenarios that predict a delay, a rapid increase, and a rapid decrease in the T-MOKE asymmetry—exactly as was observed for Ni [cf. yellow areas in Fig. 8(b)].

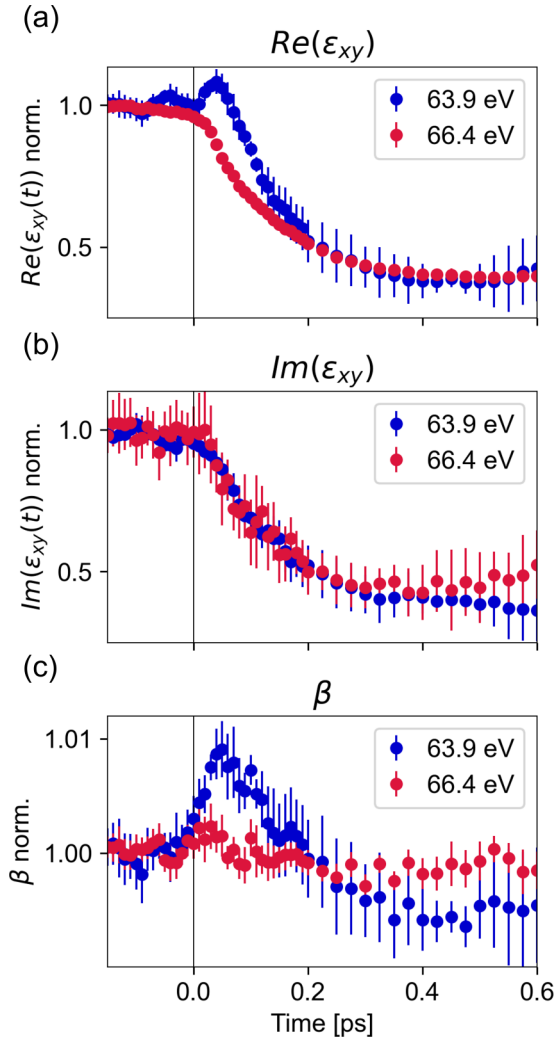


FIG. 7. [(a), (b)] Transient evolution of ε_{xy} after the optical excitation. ε_{xy} rotates in the complex plane, because the real and imaginary parts do not change identically. The rotation of ε_{xy} is of particular importance to understand the differences in the asymmetry time traces for different incidence angles below the resonance. (c) Transient changes of the imaginary part of the refractive index (β) of Ni retrieved from the angle-resolved EUV T-MOKE data. We find a strong change of β at $h\nu = 63.9$ eV that is indicative of the strong excitation of electrons. In all subplots, the error margins correspond to the statistical 1σ errors from the fits.

Furthermore, we note that a complete reversal of the T-MOKE asymmetry might also occur. A naive interpretation of the T-MOKE asymmetry might confuse this observation for a reversal of the magnetic moment, which we emphasize is not the case here. Thus, we conclude that in experiment, where the transient change of the T-MOKE asymmetry is always normalized to its value before the pump excitation, even very small angle changes of ε_{xy} can have a huge impact on the qualitative trend of the transient T-MOKE asymmetry data.

Since the T-MOKE asymmetry depends on the relative angle $\angle(\vec{p}, \vec{\varepsilon}_{xy})$, it is clear that not just a rotation of ε_{xy} but also a rotation of \vec{p}_θ might lead to unexpected dynamics in the time-resolved T-MOKE asymmetry signal. Since such rotations can arise due to changes of the refractive index,

they are commonly referred to as nonmagnetic artifacts in the ultrafast magnetism community [10,63]. However, we note that in our time-resolved analysis, β [Fig. 7(c)] and δ (Fig. 15 in Appendix A) are reconstructed in addition. Therefore, this analysis allows to separate the rotation of ε_{xy} from any rotation in \vec{p}_θ . Equivalently, this analysis separates the magnetic and nonmagnetic effects. For Ni at 64 eV, we find that the \vec{p}_θ vectors change insignificantly in comparison to ε_{xy} , indicating that the angle-dependent T-MOKE asymmetry changes are dominated by the rotation of ε_{xy} .

In summary, we find that the optically induced nonequilibrium excitation in Ni leads to a transient rotation of the off-diagonal element of the dielectric tensor. Depending on the sample structure and on the alignment of the experiment (that is, depending on the probe vector \vec{p}_θ), this rotation can lead to a relative increase, a decrease, or a delayed behavior of the T-MOKE asymmetry (see Fig. 1). In this case, the T-MOKE signal cannot be interpreted directly in terms of the magnetic moment, and care must be taken to extract the off-diagonal dielectric tensor component instead.

B. Comparison to theory

Before we carry out a direct comparison to theory, it is instructive to have a qualitative look at the resonant M -edge transitions that are probed in experiment with EUV T-MOKE spectroscopy. Figure 9(a) shows a schematic of the spin-split $3d$ and $4s$ density of states of Ni and the spin-split Ni $3p$ core levels, for which we include the approximate intrinsic linewidth broadening. As can be seen from this schematic, the spin-split $3p$ core levels overlap and cover an energy range of ≈ 5 eV, which is comparable to the energy range of the full valence and conduction band structure of Ni. Therefore, a specific EUV energy [pink arrow in Fig. 9(a)] does not only probe a specific energy within the spin-split DOS, but an extended region of several electron volts. In consequence, the collected T-MOKE asymmetry is strongly broadened, and it is not straightforward to identify spectrally resolved dynamics in the T-MOKE asymmetry or even the extracted dielectric tensor with occupation changes or band renormalizations in the electronic structure of the investigated material.

However, if we look at our TDDFT calculations in Fig. 9(b), such a comparison seems necessary at first. For 1.2 eV and 47-fs pump pulses, we find that the time-resolved change in minority and majority occupation of the DOS exhibits spectrally very distinct dynamics. For example, because of the large unoccupied DOS in the minority channel of Ni just above the Fermi level [cf. Fig. 9(a)], Fig. 9(b) shows that pumping with 1.2 eV leads to a peaked increase of minority spins in a ≈ 300 meV spectral region above the Fermi level. In other words, we see a strong minority interenergy transfer of spins from below to above the Fermi level. In the majority channel, we also pump electrons from below to above the Fermi level, but much less efficiently, because there are much fewer empty states available for the transition. In total, this means that the optical excitation leads to a magnetic moment increase below the Fermi level (loss of minority electrons), and an overall magnetic moment decrease (gain of minority electrons) just above the Fermi level. However, all of these

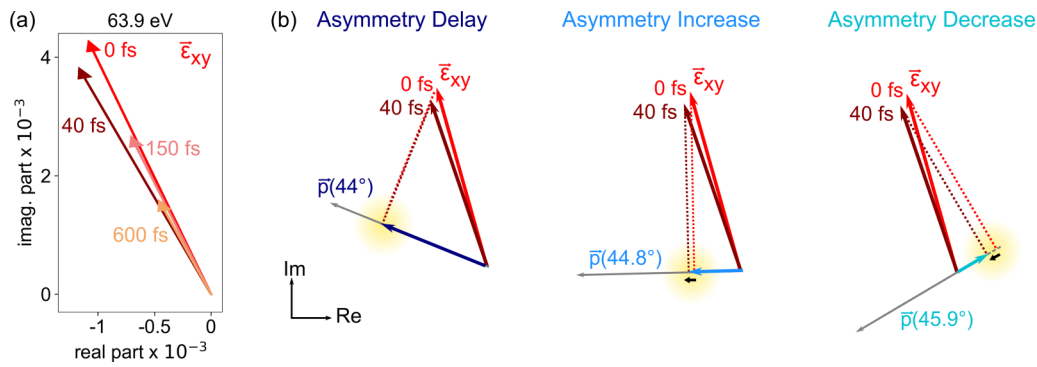


FIG. 8. (a) Transient evolution of $\bar{\epsilon}_{xy}$ for selected times after the optical excitation. $\bar{\epsilon}_{xy}$ rotates in the complex plane, as the real and imaginary parts do not change identically. (b) A rotation of $\bar{\epsilon}_{xy}$ in the complex plane can lead to an increase in, a decrease in, or no effect on the magnetic asymmetry, which can be understood from the alignment of $\bar{\epsilon}_{xy}$ and \bar{p}_θ . Here, we specifically consider the change in $\bar{\epsilon}_{xy}$ of Ni at 64 eV and 40 fs after the onset of demagnetization. At 44° , the rotation of $\bar{\epsilon}_{xy}$ is such that the projection on \bar{p}_θ does not change. Hence, no change in the magnetic asymmetry is observed. At 44.8° , the rotation leads to an increase of the projection (magnetic asymmetry), while at 45.9° , a pronounced decrease is observed. The change of the projection from $\bar{\epsilon}_{xy}$ on \bar{p}_θ between unpumped and at 40 fs is highlighted in yellow.

distinct spectral signatures will be broadened in experiment due to the large linewidth of the Ni $3p$ core levels.

We can overcome this problem by directly calculating the transient changes in the dielectric tensor, which takes all EUV

transitions into account and moreover is a quantity that we now can directly compare with experiment. Specifically, we focus on the real part of ϵ_{xy} , which can be related to the spin polarization of the unoccupied states. Figure 9(c) shows

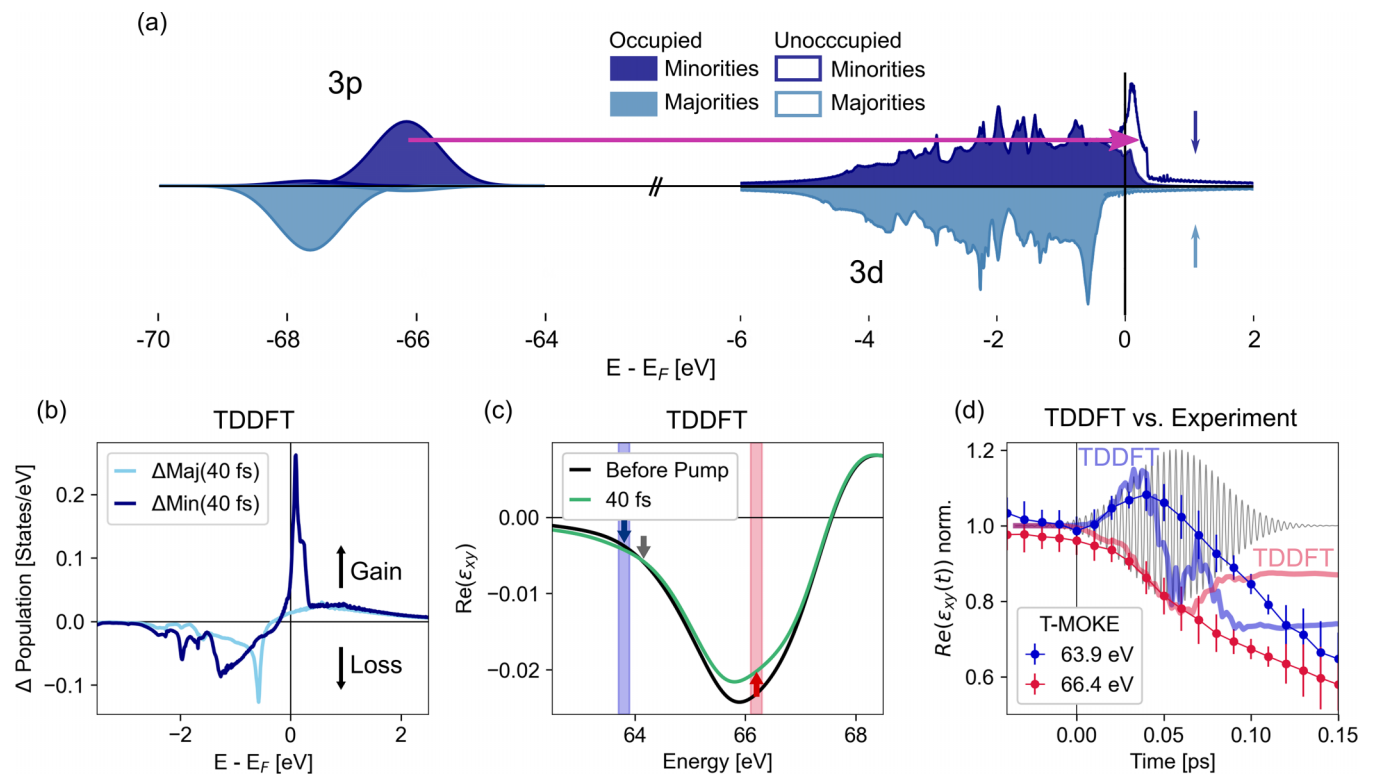


FIG. 9. Femtosecond spin dynamics from TDDFT, compared to experiment. (a) Spin-resolved density of states from density functional theory and the equilibrium occupation at 300 K for the $3p$, $3d$, and $4s$ states in Ni. Due to the exchange splitting, significantly more minority states (upper part) are unoccupied (unshaded region around E_F), thereby allowing for more optical transitions (purple arrow). (b) As seen in the population change at 40 fs, the optical excitation with 1.2 eV photons leads to a strong redistribution of the population in the minority channel (dark blue), populating empty states at 0–0.5 eV above E_F and creating empty states below E_F . In comparison, the majority channel (light blue) is less affected. (c) The redistribution of spins and charge carriers leads to a modification of the magneto-optical response (ϵ_{xy}). Depending on the position with respect to the M -edge photon energy E_M , the spectral dynamics of $\text{Re}(\epsilon_{xy})$ show regions with a strong relative decrease of $\text{Re}(\epsilon_{xy})$ (indicated with a red arrow) but also regions with a relative increase of $\text{Re}(\epsilon_{xy})$ (blue arrow) or a delayed onset of dynamics (grey arrow). (d) The calculations can be directly compared to experiment by evaluating $\text{Re}(\epsilon_{xy})$ as a function of time. Here, we observe that the predicted relative increase in $\text{Re}(\epsilon_{xy})$ is confirmed from experiment [see Fig. 6(a)]. The time axis of experiment and theory were shifted according to each, as visualized by the electric field of the pulse used for the theory calculations.

the theoretical transient dynamics of $\text{Re}(\varepsilon_{xy})$ in the corresponding energy range. First, we recognize that the spectrally distinct dynamics as seen in the transient occupation changes in Fig. 9(b) are completely smeared out. Nevertheless, we still find broad energetic regions where the interenergy spin transfer as seen in Fig. 9(b) can be verified: Below the energy marked with the grey arrow in Fig. 9(c), $\text{Re}(\varepsilon_{xy})$ shows an ultrafast relative increase, and an ultrafast decrease for energies above. If $\text{Re}(\varepsilon_{xy})$ would be extracted exactly at the energy of the green arrow, we would expect a delayed behavior in the dynamics.

Having this theoretical result on transient dynamics of $\text{Re}(\varepsilon_{xy})$, we now carry out a direct comparison with experiment, where we were able to extract $\text{Re}(\varepsilon_{xy})$ at the energies marked with blue and red shaded areas in Fig. 9(c). Figure 9(d) shows this comparison of time-resolved dynamics of $\text{Re}(\varepsilon_{xy})$ for theory (solid lines) and experiment (data points). Clearly, the predicted relative increase and decrease in $\text{Re}(\varepsilon_{xy})$ after optical pumping can be confirmed. The initial increase of $\text{Re}(\varepsilon_{xy})$ at 64 eV reflects that more minority than majority spins are excited from below the Fermi level. This also agrees with the measured dynamics of the nonmagnetic elements of the dielectric tensor, namely, that the absorption increases for the photon energy of 64 eV [cf. Fig. 7(c)] as the optical excitation of the pump leads to available empty states below the Fermi level. We also find that for longer time delays > 100 fs, the experimental data show a further reduction of $\text{Re}(\varepsilon_{xy})$, while the theory data stay constant. This is to be expected, because long-range interactions such as phonon and magnon generation are not taken into account in the TDDFT calculation, which in experiment contribute to the demagnetization of the sample on timescales larger than 100 fs.

In summary, TDDFT predicts an OISTR-like process, i.e., an optically driven interenergy spin transfer similar to the intersite spin transfer in the usual OISTR process. This pumping of spins happens predominantly in the minority channel and leads to distinct spectrally dependent magnetization increase and decrease below and above the Fermi level, respectively. Via a direct calculation of the real part of the off-diagonal element of the dielectric tensor, $\text{Re}(\varepsilon_{xy})$, we are able to pinpoint the interenergy transfer in the transient dynamics of $\text{Re}(\varepsilon_{xy})$. As $\text{Re}(\varepsilon_{xy})$ can be directly extracted from our experimental data, we are able to unambiguously verify the optically driven interenergy spin-transfer process in Ni.

C. Implications for EUV T-MOKE

Now that we have analyzed the strongly angle-dependent transient T-MOKE signals in nickel, and interpreted them in terms of an unbalanced excitation of minority carriers on the few-femtosecond scale, it is necessary to discuss how this affects the validity of EUV T-MOKE as an experimental technique. At first sight, the possibility for ε_{xy} to rotate and the resulting dramatically different experimental data (Fig. 1) might imply that T-MOKE is not suitable to trace the energy- or even element-resolved magnetic moment on the femtosecond scale. The situation is not so dramatic, however; while our measurements certainly show that there exist situations where pure T-MOKE does not suffice, there are many situations where it gives an accurate view on the magnetization

dynamics. We find that these situations can to first order be distinguished by the vectorial picture of $\vec{\varepsilon}_{xy}$ and \vec{p}_θ (Figs. 3 and 8). The rotation of ε_{xy} is most important when these vectors are close to perpendicular, while for (near) parallel alignment, mostly the magnitude of ε_{xy} is measured. Furthermore, regions of perpendicular and parallel alignment can easily be distinguished even without calculation, as perpendicular alignment of ε_{xy} and \vec{p}_θ is the dominant reason for zero crossings in the T-MOKE asymmetry, whereas the maxima of the asymmetry coincide with parallel alignment. Consequently, T-MOKE data that are evaluated in an energy range around the maximum of the asymmetry are generally insensitive to rotations and can thus be trusted, while T-MOKE data that are recorded off-resonance near zero crossings are much more susceptible to such effects and should thus be examined carefully. In this context, it is very important to realize that our experimental evidence of rotating ε_{xy} is not only crucial for the correct analysis of T-MOKE data, but must also be considered in the analysis of data recorded with any other time-resolved magneto-optical technique.

Although the sensitivity to rotations of ε_{xy} implies that femtosecond magneto-optical data must be analyzed more carefully, this sensitivity also presents a valuable opportunity. In Sec. III, we have shown how data on the full dielectric tensor can be efficiently extracted from angle-resolved T-MOKE data. This enables several benefits over the conventional T-MOKE analysis. At a basic level, by discerning rotation from changes in the magnitude of ε_{xy} , the angle-resolved analysis directly identifies the spectral regions where T-MOKE requires a more careful analysis. More importantly, given a good understanding of the sample properties including film thickness and refractive index, the angle-resolved data directly enable this careful analysis, and are able to provide quantitative data not only on the complex-valued ε_{xy} , but also on the nonmagnetic response ε_{xx} . It is important to realize that this enables a complete disentanglement of the magnetic and the electronic response of the sample to an optical excitation. Hence, the analyzed ultrafast magnetization data become “artifact-free.” We expect that this capability will be highly relevant for optically driven magnetization dynamics, such as in the OISTR process.

Light-driven femtosecond magnetization dynamics, and particularly the OISTR process, are prime examples of where the angle-resolved analysis can improve our understanding. This is because light, particularly at optical frequencies, induces a redistribution of electrons in the spin-resolved band structure, generally leading to a nonthermal occupation and thereby affecting the full dielectric tensor. In fact, we deem it essential to revisit the OISTR process in FeNi alloys, which after all was first verified with the T-MOKE experiment [22]. In that experiment, the T-MOKE data of an Fe₅₀Ni₅₀ alloy showed a spectrally dependent increase in magnetic asymmetry in Ni and a concomitant decrease in Fe. As our analysis suggests the possibility that these T-MOKE data were the result of a rotation of ε_{xy} , it is necessary to perform an angle-resolved analysis to validate the theoretically predicted OISTR. In Ref. [64] we perform such a study, where we make use of the ε_{xy} analysis of the present work and discuss the implications for OISTR in FeNi alloys.

V. CONCLUSION

In conclusion, we have discussed an intriguing effect in EUV T-MOKE magnetism studies, where different transient dynamics were observed under almost identical experimental conditions. This observation conclusively illustrates that it is not always possible to directly compare time-resolved T-MOKE data and magneto-optical data in general with time-resolved calculations of the spin-resolved density of states. Here, we show that a quantitative comparison with TDDFT can be achieved by extracting the transient dynamics of the off-axis dielectric tensor element ε_{xy} .

We have presented a robust technique to retrieve ε_{xy} from experimental T-MOKE data with full femtosecond time resolution at little experimental cost. The data that we have achieved solve the controversy that slightly different incidence angles lead to dramatically different dynamics in the T-MOKE asymmetry. Even more, our technique allows to directly reconstruct and fully disentangle the magnetic and nonmagnetic parts of the refractive index. Studying the prototypical case of femtosecond demagnetization in Ni, we show that these data are ideal for a quantitative analysis and comparison with TDDFT calculations and allow to trace the optically induced spin and charge dynamics in exceptional detail. We want to emphasize that besides a comparison of the same quantity, i.e., ε_{xy} , this approach also ensures that spectral broadening, multiple edges, and overlapping edges from multiple elements in multicomponent materials are properly taken into account.

The supporting data and analysis scripts for this article are openly available from GRO.Data [65].

ACKNOWLEDGMENTS

We thank Natalie Jacqueline Ottinger for her assistance in the x-ray reflectivity evaluation and Tim Titze for the finite-difference time-domain simulations. This work was funded by the Deutsche Forschungsgemeinschaft (DFG, German Research Foundation), Project IDs 399572199 and 432680300/SFB 1456. G.S.M.J. acknowledges financial support by the Alexander von Humboldt Foundation. S.S. and J.K.D. would like to thank the DFG for funding through Project ID 328545488 TRR227 (Project A04).

APPENDIX A: EXPERIMENTAL SETUP AND ANALYSIS DETAILS

The experimental setup used for the determination of the time-resolved dielectric tensor is based on the EUV T-MOKE setup that was described in Ref. [31]. We pumped the samples with a 47 ± 5 fs pulse [Gauss full width at half maximum (FWHM)] with a photon energy of 1.2 eV. The absorbed fluence for the measurements was 0.8 ± 0.2 mJ/cm². The reflected 100-kHz EUV probe beam spans energies in the range of 30–72 eV. For the data acquisition at different angles of incidence (see Fig. 10), an accurate and repeatable control of the incidence angle was ensured by mounting the sample on a small nonmagnetic, UHV-compatible tip-tilt stage (SmarAct GmbH, STT-12.7-UHVT-NM; Fig. 10).

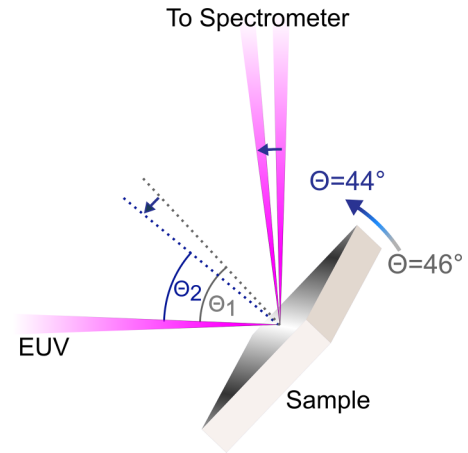


FIG. 10. Schematic of the T-MOKE experiment. A small, non-magnetic tip-tilt holder enables repeatable control of the incidence angle in a range of 2.5° around 45°.

Prior to the experiment, the sample composition was verified using an x-ray reflectivity measurement (D8 Discover, Bruker). The x-ray reflectivity data were analyzed using the DIFFRAC.LEPTOS software package by Bruker. The retrieved parameters of the nickel oxide, nickel, and silicon nitride layers are given in Table I. To verify that the sample will be demagnetized homogeneously by the femtosecond laser pulse, we performed finite-difference time-domain simulations (see Fig. 11). From these calculations, we observe that the electron temperature is homogeneous over most of the Ni film thickness, and only decreases in the bottom 5 nm. Although such a temperature difference can lead to inhomogeneous magnetization profiles influenced by superdiffusive spin currents [62], we note that this effect is limited because of the insulating substrate.

After reflection from the sample, the EUV light is analyzed in the EUV spectrometer. A typical spectrum is shown in Fig. 12. The energy axis of our spectrometer is determined from the spacing of the high-order harmonics, which is given by twice the fundamental photon energy of 1.2 eV. This leads to a relative uncertainty of <2% on the photon energy calibration. From the energy-resolved dynamics, we estimate the spectral resolution to be better than 0.2 eV.

For the determination of the off-diagonal dielectric tensor ε_{xy} from T-MOKE data, the asymmetry was evaluated in 0.1 eV energy windows separated by 0.3 eV (center to center) at energies close to the high-order harmonic maxima. Fit results of the static magnetic asymmetries for the extraction of ε_{xy} (Sec. III A) together with the observed T-MOKE asymmetry are shown in Fig. 13 and yield good agreement with the

TABLE I. Fit results of the x-ray reflectivity measurement.

	Thickness (nm)	Roughness (nm)	Density (g/cm ³)
NiO	2.0 ± 0.6	0.4 ± 1.1	6.2 ± 0.4
Ni	21.9 ± 0.7	1.9 ± 0.4	9.0 ± 0.1
Si ₃ N ₄	112 ± 2	2.0 ± 0.4	3.19 (fixed)

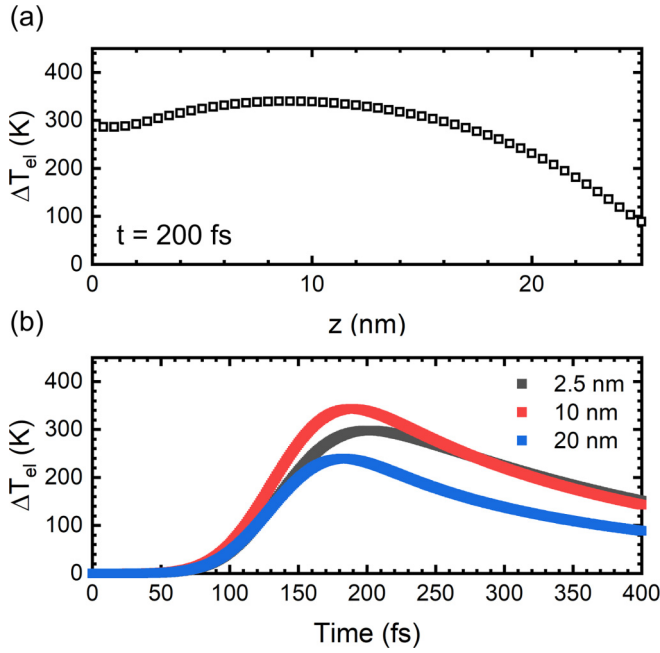


FIG. 11. Finite-difference time-domain simulations of the electron temperature in a NiO (2 nm)/Ni (22 nm)/Si₃N₄ sample at $t = 200$ fs.

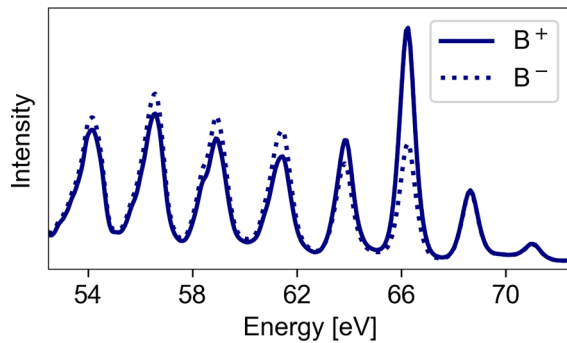


FIG. 12. Typical high-order harmonic spectrum after the reflection from the Ni thin film for opposite magnetization directions. The discrete nature of the spectrum of odd harmonics of the fundamental beam is clearly visible. The magneto-optical response is largest around the Ni resonance at ≈ 66 eV, which is visible by the large difference in intensity for opposite magnetization directions.

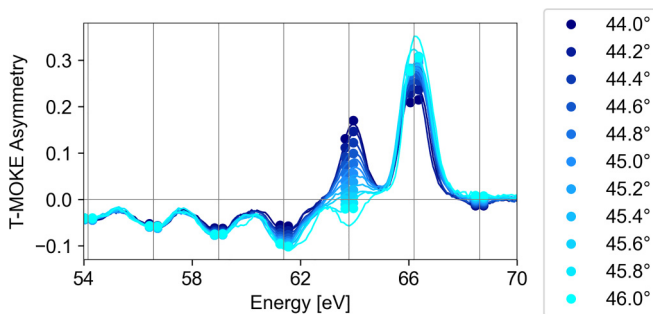


FIG. 13. Fit of the static magnetic asymmetries for the extraction of ϵ_{xy} as described in Sec. III A. The results from the fit procedure (colored circles) provide a satisfactory description of the experimental data (solid lines).

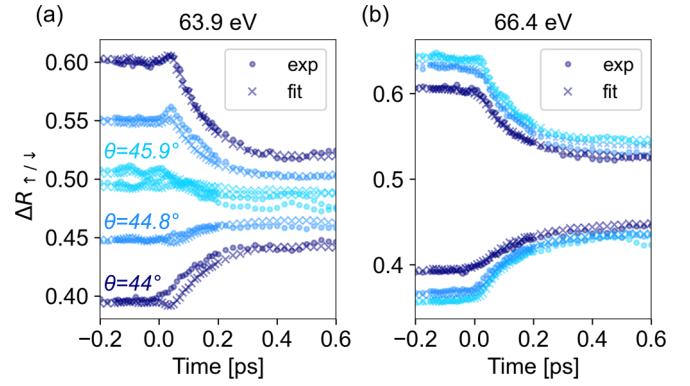


FIG. 14. Time-resolved analysis of the dielectric tensor, if transient changes of the refractive index in the sample are neglected. The panels show the measured (points) and reconstructed (line) transient relative reflectivity $\Delta R_{\uparrow/\downarrow}(t)$ for opposite magnetization directions [cf. Eq. (7) in the main text] during optically induced demagnetization for photon energies (a) just below and (b) close to the Ni M edge—equivalent to Figs. 6(a) and 6(b) in the main text. The exclusion of transient optical changes of the refractive index results in a poor fit of the experimental data, especially at the energy below the resonance, where the $\Delta R_{\uparrow/\downarrow}(t)$ curves deviate from the usual mirror-symmetric behavior. At this energy, the excitation of electrons by the laser pulse is most dominant and has a strong effect on the refractive index.

measured static T-MOKE asymmetries. We note that the T-MOKE asymmetry is strongly reduced in between high-order harmonic energies due to the comparably higher background contribution at those energies.

The transient evolution of the off-diagonal dielectric tensor ϵ_{xy} was determined from the measured reflectivities $R_{\uparrow/\downarrow}$ (Sec. III C). For the fitting of $R_{\uparrow/\downarrow}$, good agreement with the experimental data on early timescales can only be achieved by the inclusion of transient optical changes of the complex refractive index $n = 1 - \delta + i\beta$. In particular, this is important below the resonance (around ≈ 64 eV), where we probe states below E_F , which are most strongly affected by the excitation of electrons by the pump pulse. Not including the refractive index changes yields a poor agreement between the measured $R_{\uparrow/\downarrow}$ and the fit, as shown in Fig. 14. The extracted transient evolution of the real and imaginary part of the off-diagonal dielectric tensor element ϵ_{xy} and the optical changes of δ and β for selected energies around the Ni resonance are shown in Fig. 15.

We performed a full time-resolved ϵ_{xy} analysis for several thicknesses of the NiO capping layer (1.5, 2, and 2.5 nm), and found that the qualitative experimental result of our study on Ni (namely, that more minority spins are pumped from below the Fermi level) does not change. Notably, we observe that increasing the NiO layer thickness leads to an apparent reduction of the static value at $\text{Re}(\epsilon_{xy})$ at 64 eV. In the dynamics, the strength of the rotation remains similar, which then implies a stronger relative increase when $\text{Re}(\epsilon_{xy})$ is smaller. For 1.5-nm NiO, we find a 4% increase, for 2-nm NiO an 8% increase, and for 2.5-nm NiO 33% (see Fig. 16).

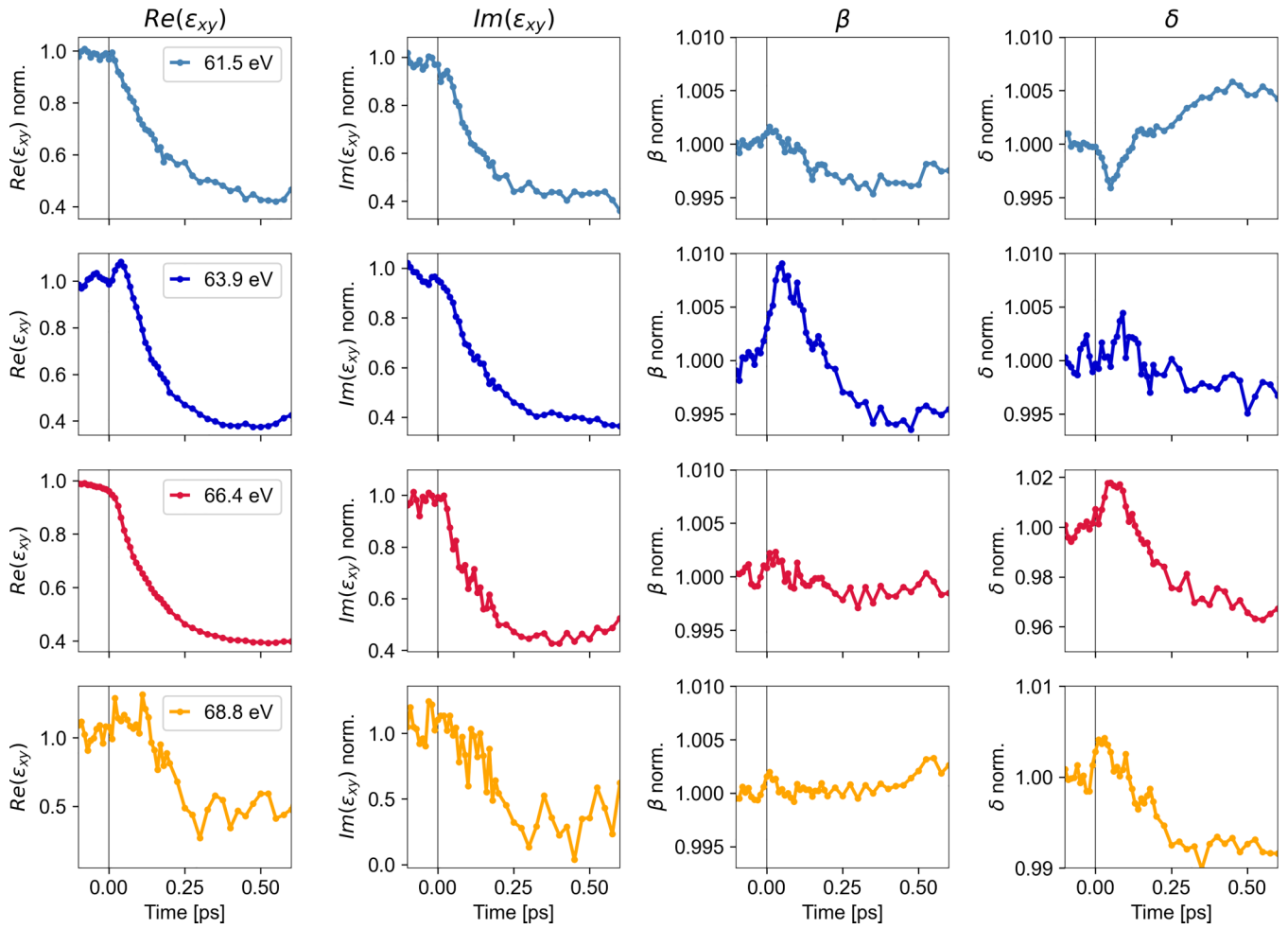


FIG. 15. Fit results of the transient behavior of ϵ_{xy} and n for different energies around the Ni M edge.

APPENDIX B: TIME-DEPENDENT DENSITY FUNCTIONAL THEORY

For the TDDFT calculations a pump pulse with a central photon energy of 1.2 eV, a Gaussian intensity profile with FWHM = 47 fs, and an incident fluence of ≈ 18 mJ/cm² was used.

The comparison between experiment and TDDFT focuses on the short timescale, below 100 fs, and there are discrepancies for the longer timescale as TDDFT does not include all processes relevant for ultrafast demagnetization. The following processes have been included in the TDDFT calculation: (a) spin and charge currents due to laser excitation, (b) spin-orbit-induced spin flips, (c) effect of these spin flips on the

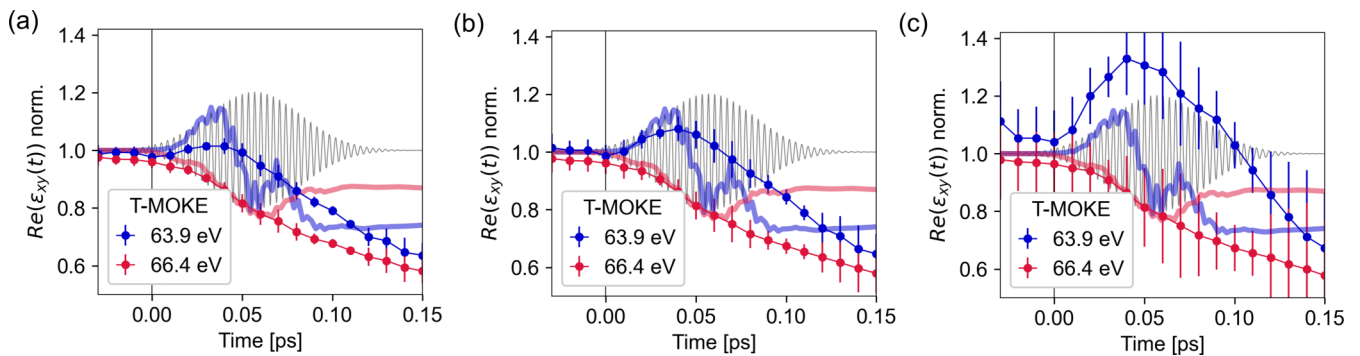


FIG. 16. Reconstructed ϵ_{xy} dynamics for three different assumed NiO thicknesses. (a) For 1.5-nm NiO, we find a 4% increase; (b) for 2-nm NiO, an 8% increase; and (c) for 2.5-nm NiO, 33%. The increased amplitude is directly related to a reduction of the value of $\text{Re}(\epsilon_{xy})$ before excitation. Qualitative agreement with TDDFT is found in all cases.

spin currents [66], (d) electron-electron scattering effects via the exchange-correlation functional, and (e) coupling of the electrons to nuclear degrees of freedom; this coupling implies that the momentum is allowed to flow from spin and orbital degrees of freedom to nuclei. In contrast, second-order effects are missing in our simulations which then can displace nuclei (i.e., to generate phonons), and this, in turn, causes charge and

spin densities to change. Thus, spin flips via electron-phonon scattering are not included. Since the calculations are performed for the bulk, the effects of substrate like superdiffusive spin currents are not included. Magnon generation is also not included. For more details of the method and the code see Refs. [46,59,67].

-
- [1] E. Beaurepaire, J.-C. Merle, A. Daunois, and J.-Y. Bigot, Ultrafast spin dynamics in ferromagnetic nickel, *Phys. Rev. Lett.* **76**, 4250 (1996).
- [2] A. Kirilyuk, A. V. Kimel, and T. Rasing, Ultrafast optical manipulation of magnetic order, *Rev. Mod. Phys.* **82**, 2731 (2010).
- [3] J.-Y. Bigot, M. Vomir, and E. Beaurepaire, Coherent ultrafast magnetism induced by femtosecond laser pulses, *Nat. Phys.* **5**, 515 (2009).
- [4] B. Koopmans, M. van Kampen, J. T. Kohlhepp, and W. J. M. de Jonge, Ultrafast magneto-optics in nickel: Magnetism or optics?, *Phys. Rev. Lett.* **85**, 844 (2000).
- [5] L. Guidoni, E. Beaurepaire, and J.-Y. Bigot, Magneto-optics in the ultrafast regime: Thermalization of spin populations in ferromagnetic films, *Phys. Rev. Lett.* **89**, 017401 (2002).
- [6] P. M. Oppeneer and A. Liebsch, Ultrafast demagnetization in Ni: Theory of magneto-optics for non-equilibrium electron distributions, *J. Phys.: Condens. Matter* **16**, 5519 (2004).
- [7] G. P. Zhang, W. Hübner, G. Lefkidis, Y. Bai, and T. F. George, Paradigm of the time-resolved magneto-optical Kerr effect for femtosecond magnetism, *Nat. Phys.* **5**, 499 (2009).
- [8] K. Carva, M. Battiato, and P. M. Oppeneer, Is the controversy over femtosecond magneto-optics really solved?, *Nat. Phys.* **7**, 665 (2011).
- [9] K. Carva, D. Legut, and P. M. Oppeneer, Influence of laser-excited electron distributions on the x-ray magnetic circular dichroism spectra: Implications for femtosecond demagnetization in Ni, *Europhys. Lett.* **86**, 57002 (2009).
- [10] C. La-O-Vorakiat, E. Turgut, C. A. Teale, H. C. Kapteyn, M. M. Murnane, S. Mathias, M. Aeschlimann, C. M. Schneider, J. M. Shaw, H. T. Nembach, and T. J. Silva, Ultrafast demagnetization measurements using extreme ultraviolet light: Comparison of electronic and magnetic contributions, *Phys. Rev. X* **2**, 011005 (2012).
- [11] W. Zhang, P. Maldonado, Z. Jin, T. S. Seifert, J. Arabski, G. Schmerber, E. Beaurepaire, M. Bonn, T. Kampfthath, P. M. Oppeneer, and D. Turchinovich, Ultrafast terahertz magnetometry, *Nat. Commun.* **11**, 4247 (2020).
- [12] B. T. Thole, P. Carra, F. Sette, and G. van der Laan, X-ray circular dichroism as a probe of orbital magnetization, *Phys. Rev. Lett.* **68**, 1943 (1992).
- [13] C. La-O-Vorakiat, M. Siemens, M. M. Murnane, H. C. Kapteyn, S. Mathias, M. Aeschlimann, P. Grychtol, R. Adam, C. M. Schneider, J. M. Shaw, H. Nembach, and T. J. Silva, Ultrafast demagnetization dynamics at the *M* edges of magnetic elements observed using a tabletop high-harmonic soft x-ray source, *Phys. Rev. Lett.* **103**, 257402 (2009).
- [14] B. Vodungbo, J. Gautier, G. Lambert, A. B. Sardinha, M. Lozano, S. Sebban, M. Ducouso, W. Boutu, K. Li, B. Tudu, M. Tortarolo, R. Hawaldar, R. Delaunay, V. López-Flores, J. Arabski, C. Boeglin, H. Merdji, P. Zeitoun, and J. Lüning, Laser-induced ultrafast demagnetization in the presence of a nanoscale magnetic domain network, *Nat. Commun.* **3**, 999 (2012).
- [15] C. Alves, G. Lambert, V. Malka, M. Hehn, G. Malinowski, M. Hennes, V. Chardonnet, E. Jal, J. Lüning, and B. Vodungbo, Resonant Faraday effect using high-order harmonics for the investigation of ultrafast demagnetization, *Phys. Rev. B* **100**, 144421 (2019).
- [16] I. Kumberg, E. Golias, S. E. Hadjadj, R. Hosseinifar, S. Thakur, T. Shinwari, I. Gelen, N. Pontius, C. Schüßler-Langeheine, C. von Korff Schmising, S. Sharma, and W. Kuch, Ultrafast laser-induced magneto-optical changes in resonant magnetic x-ray reflectivity, *Phys. Rev. B* **108**, 054439 (2023).
- [17] S. Mathias, C. La-O-Vorakiat, P. Grychtol, P. Granitzka, E. Turgut, J. M. Shaw, R. Adam, H. T. Nembach, M. E. Siemens, S. Eich *et al.*, Probing the timescale of the exchange interaction in a ferromagnetic alloy, *Proc. Natl. Acad. Sci. USA* **109**, 4792 (2012).
- [18] B. Pfau, S. Schaffert, L. Müller, C. Gutt, A. Al-Shemmary, F. Büttner, R. Delaunay, S. Düsterer, S. Flewett, R. Frömter *et al.*, Ultrafast optical demagnetization manipulates nanoscale spin structure in domain walls, *Nat. Commun.* **3**, 1100 (2012).
- [19] D. Rudolf, C. La-O-Vorakiat, M. Battiato, R. Adam, J. M. Shaw, E. Turgut, P. Maldonado, S. Mathias, P. Grychtol, H. T. Nembach *et al.*, Ultrafast magnetization enhancement in metallic multilayers driven by superdiffusive spin current, *Nat. Commun.* **3**, 1037 (2012).
- [20] E. Turgut, C. La-o-vorakiat, J. M. Shaw, P. Grychtol, H. T. Nembach, D. Rudolf, R. Adam, M. Aeschlimann, C. M. Schneider, T. J. Silva, M. M. Murnane, H. C. Kapteyn, and S. Mathias, Controlling the competition between optically induced ultrafast spin-flip scattering and spin transport in magnetic multilayers, *Phys. Rev. Lett.* **110**, 197201 (2013).
- [21] F. Willems, C. von Korff Schmising, C. Strüber, D. Schick, D. W. Engel, J. K. Dewhurst, P. Elliott, S. Sharma, and S. Eisebitt, Optical inter-site spin transfer probed by energy and spin-resolved transient absorption spectroscopy, *Nat. Commun.* **11**, 871 (2020).
- [22] M. Hofherr, S. Häuser, J. K. Dewhurst, P. Tengdin, S. Sakshath, H. T. Nembach, S. T. Weber, J. M. Shaw, T. J. Silva, H. C. Kapteyn, M. Cinchetti, B. Rethfeld, M. M. Murnane, D. Steil, B. Stadtmüller, S. Sharma, M. Aeschlimann, and S. Mathias, Ultrafast optically induced spin transfer in ferromagnetic alloys, *Sci. Adv.* **6**, eaay8717 (2020).
- [23] P. Tengdin, C. Gentry, A. Blonsky, D. Zusin, M. Gerrity, L. Hellbrück, M. Hofherr, J. Shaw, Y. Kvashnin, E. K. Delczeg-Czirjak, M. Arora, H. Nembach, T. J. Silva, S. Mathias, M. Aeschlimann, H. C. Kapteyn, D. Thonig, K. Koumpouras,

- O. Eriksson, and M. M. Murnane, Direct light-induced spin transfer between different elements in a spintronic Heusler material via femtosecond laser excitation, *Sci. Adv.* **6**, eaaz1100 (2020).
- [24] M. Hennecke, D. Schick, T. Sidiropoulos, F. Willems, A. Heilmann, M. Bock, L. Ehrentraut, D. Engel, P. Helsing, B. Pfau *et al.*, Ultrafast element- and depth-resolved magnetization dynamics probed by transverse magneto-optical Kerr effect spectroscopy in the soft x-ray range, *Phys. Rev. Res.* **4**, L022062 (2022).
- [25] O. Kfir, S. Zayko, C. Nolte, M. Sivis, M. Möller, B. Hebler, S. S. P. K. Arekapudi, D. Steil, S. Schäfer, M. Albrecht, O. Cohen, S. Mathias, and C. Ropers, Nanoscale magnetic imaging using circularly polarized high-harmonic radiation, *Sci. Adv.* **3**, eaao4641 (2017).
- [26] S. Zayko, O. Kfir, M. Heigl, M. Lohmann, M. Sivis, M. Albrecht, and C. Ropers, Ultrafast high-harmonic nanoscopy of magnetization dynamics., *Nat. Commun.* **12**, 6337 (2020).
- [27] S. A. Ryan, P. C. Johnsen, M. F. Elhanoty, A. Grafov, N. Li, A. Delin, A. Markou, E. Lesne, C. Felser, O. Eriksson, H. C. Kapteyn, O. Grånäs, and M. M. Murnane, Optically controlling the competition between spin flips and intersite spin transfer in a Heusler half-metal on sub-100 fs timescales, *Sci. Adv.* **9**, eadi1428 (2023).
- [28] S. Jana, J. A. Terschlüsen, R. Stefanuik, S. Plogmaker, S. Troisi, R. S. Malik, M. Svanqvist, R. Knut, J. Söderström, and O. Karis, A setup for element specific magnetization dynamics using the transverse magneto-optic Kerr effect in the energy range of 30-72 eV, *Rev. Sci. Instrum.* **88**, 033113 (2017).
- [29] M. Hofherr, S. Moretti, J. Shim, S. Häuser, N. Y. Safonova, M. Stiehl, A. Ali, S. Sakshath, J. W. Kim, D. H. Kim, H. J. Kim, J. I. Hong, H. C. Kapteyn, M. M. Murnane, M. Cinchetti, D. Steil, S. Mathias, B. Stadtmüller, M. Albrecht, D. E. Kim, U. Nowak, and M. Aeschlimann, Induced versus intrinsic magnetic moments in ultrafast magnetization dynamics, *Phys. Rev. B* **98**, 174419 (2018).
- [30] K. Yao, F. Willems, C. von Korff Schmising, C. Strüber, P. Helsing, B. Pfau, D. Schick, D. Engel, K. Gerlinger, M. Schneider *et al.*, A tabletop setup for ultrafast helicity-dependent and element-specific absorption spectroscopy and scattering in the extreme ultraviolet spectral range, *Rev. Sci. Instrum.* **91**, 093001 (2020).
- [31] C. Möller, H. Probst, J. Otto, K. Stroh, C. Mahn, S. Steil, V. Moshnyaga, G. S. M. Jansen, D. Steil, and S. Mathias, Ultrafast element-resolved magneto-optics using a fiber-laser-driven extreme ultraviolet light source, *Rev. Sci. Instrum.* **92**, 065107 (2021).
- [32] P. C. Johnsen, S. A. Ryan, C. Gentry, A. Grafov, H. Kapteyn, and M. Murnane, A beamline for ultrafast extreme ultraviolet magneto-optical spectroscopy in reflection near the shot noise limit, *Rev. Sci. Instrum.* **94**, 033001 (2023).
- [33] J. K. Dewhurst, P. Elliott, S. Shallcross, E. K. U. Gross, and S. Sharma, Laser-induced intersite spin transfer, *Nano Lett.* **18**, 1842 (2018).
- [34] F. Siegrist, J. A. Gessner, M. Ossiander, C. Denker, Y.-P. Chang, M. C. Schröder, A. Guggenmos, Y. Cui, J. Walowski, U. Martens, J. K. Dewhurst, U. Kleineberg, M. Münzenberg, S. Sharma, and M. Schultze, Light-wave dynamic control of magnetism, *Nature (London)* **571**, 240 (2019).
- [35] S. Jana, R. S. Malik, Y. O. Kvashnin, I. L. Locht, R. Knut, R. Stefanuik, I. Di Marco, A. Yaresko, M. Ahlberg, J. Åkerman *et al.*, Analysis of the linear relationship between asymmetry and magnetic moment at the M edge of $3d$ transition metals, *Phys. Rev. Res.* **2**, 013180 (2020).
- [36] I. Radu, C. Stamm, A. Eschenlohr, F. Radu, R. Abrudan, K. Vahaplar, T. Kachel, N. Pontius, R. Mitzner, K. Holldack, A. Föhlisch, T. A. Ostler, J. H. Mentink, R. F. L. Evans, R. W. Chantrell, A. Tsukamoto, A. Itoh, A. Kirilyuk, A. V. Kimel, and T. Rasing, Ultrafast and distinct spin dynamics in magnetic alloys, *SPIN* **05**, 1550004 (2015).
- [37] F. Willems, S. Sharma, C. von Korff Schmising, J. K. Dewhurst, L. Salemi, D. Schick, P. Helsing, C. Strüber, W. D. Engel, and S. Eisebitt, Magneto-optical functions at the $3p$ resonances of Fe, Co, and Ni: *Ab initio* description and experiment, *Phys. Rev. Lett.* **122**, 217202 (2019).
- [38] J. K. Dewhurst, F. Willems, P. Elliott, Q. Z. Li, C. von Korff Schmising, C. Strüber, D. W. Engel, S. Eisebitt, and S. Sharma, Element specificity of transient extreme ultraviolet magnetic dichroism, *Phys. Rev. Lett.* **124**, 077203 (2020).
- [39] J. L. Erskine and E. A. Stern, Calculation of the $M_{2,3}$ magneto-optical absorption spectrum of ferromagnetic nickel, *Phys. Rev. B* **12**, 5016 (1975).
- [40] E. Runge and E. K. U. Gross, Density-functional theory for time-dependent systems, *Phys. Rev. Lett.* **52**, 997 (1984).
- [41] R. Van Leeuwen, Key concepts in time-dependent density-functional theory, *Int. J. Mod. Phys. B* **15**, 1969 (2001).
- [42] S. Sharma, J. K. Dewhurst, and E. K. U. Gross, Optical response of extended systems using time-dependent density functional theory, in *First Principles Approaches to Spectroscopic Properties of Complex Materials* (Springer, Berlin, 2014), pp. 235–257.
- [43] P. M. Oppeneer, T. Maurer, J. Sticht, and J. Kübler, *Ab initio* calculated magneto-optical Kerr effect of ferromagnetic metals: Fe and Ni, *Phys. Rev. B* **45**, 10924 (1992).
- [44] P. Oppeneer, Magneto-optical Kerr spectra, in *Handbook of Magnetic Materials*, edited by K. H. J. Buschow (Elsevier, Amsterdam, 2001), pp. 229–422.
- [45] J. Kuneš, P. M. Oppeneer, H.-C. Mertins, F. Schäfers, A. Gaupp, W. Gudat, and P. Novák, X-ray Faraday effect at the $L_{2,3}$ edges of Fe, Co, and Ni: Theory and experiment, *Phys. Rev. B* **64**, 174417 (2001).
- [46] K. Krieger, J. Dewhurst, P. Elliott, S. Sharma, and E. Gross, Laser-induced demagnetization at ultrashort time scales: Predictions of TDDFT, *J. Chem. Theory Comput.* **11**, 4870 (2015).
- [47] D. Zusin, P. M. Tengdin, M. Gopalakrishnan, C. Gentry, A. Blonsky, M. Gerrity, D. Legut, J. M. Shaw, H. T. Nembach, T. J. Silva, P. M. Oppeneer, H. C. Kapteyn, and M. M. Murnane, Direct measurement of the static and transient magneto-optical permittivity of cobalt across the entire M -edge in reflection geometry by use of polarization scanning, *Phys. Rev. B* **97**, 024433 (2018).
- [48] S. Mathias, J. M. Shaw, E. Turgut, P. Grychtol, R. Adam, D. Rudolf, H. T. Nembach, T. J. Silva, M. Aeschlimann, C. M. Schneider *et al.*, Ultrafast element-specific magnetization dynamics of complex magnetic materials on a table-top, *J. Electron Spectrosc. Relat. Phenom.* **189**, 164 (2013).
- [49] E. Turgut, D. Zusin, D. Legut, K. Carva, R. Knut, J. M. Shaw, C. Chen, Z. Tao, H. T. Nembach, T. J. Silva *et al.*, Stoner versus Heisenberg: Ultrafast exchange reduction and magnon

- generation during laser-induced demagnetization, *Phys. Rev. B* **94**, 220408(R) (2016).
- [50] J. Zak, E. Moog, C. Liu, and S. Bader, Universal approach to magneto-optics, *J. Magn. Magn. Mater.* **89**, 107 (1990).
- [51] J. Zak, E. R. Moog, C. Liu, and S. D. Bader, Magneto-optics of multilayers with arbitrary magnetization directions, *Phys. Rev. B* **43**, 6423 (1991).
- [52] D. Schick, A. Bojahr, M. Herzog, R. Shayduk, C. von Korff Schmising, and M. Bargheer, UDKM1DSIM—A simulation toolkit for 1D ultrafast dynamics in condensed matter, *Comput. Phys. Commun.* **185**, 651 (2014).
- [53] A. Meurer, C. P. Smith, M. Paprocki, O. Čertík, S. B. Kirpichev, M. Rocklin, A. Kumar, S. Ivanov, J. K. Moore, S. Singh, T. Rathnayake, S. Vig, B. E. Granger, R. P. Muller, F. Bonazzi, H. Gupta, S. Vats, F. Johansson, F. Pedregosa, M. J. Curry, A. R. Terrel, v. Roučka, A. Saboo, I. Fernando, S. Kulal, R. Cimrman, and A. Scopatz, SymPy: Symbolic computing in Python, *PeerJ Comput. Sci.* **3**, e103 (2017).
- [54] H. Höchst, D. Rioux, D. Zhao, and D. L. Huber, Magnetic linear dichroism effects in reflection spectroscopy: A case study at the Fe $M_{2,3}$ edge, *J. Appl. Phys.* **81**, 7584 (1997).
- [55] S. Valencia, A. Gaupp, W. Gudat, H.-C. Mertins, P. M. Oppeneer, D. Abramssohn, and C. M. Schneider, Faraday rotation spectra at shallow core levels: $3p$ edges of Fe, Co, and Ni, *New J. Phys.* **8**, 254 (2006).
- [56] C. Gutt, T. Sant, D. Ksenzov, F. Capotondi, E. Pedersoli, L. Raimondi, I. P. Nikolov, M. Kiskinova, S. Jaiswal, G. Jakob, M. Kläui, H. Zabel, and U. Pietsch, Probing ultrafast changes of spin and charge density profiles with resonant XUV magnetic reflectivity at the free-electron laser FERMI, *Struct. Dyn.* **4**, 055101 (2017).
- [57] V. Chardonnet, M. Hennes, R. Jarrier, R. Delaunay, N. Jaouen, M. Kuhlmann, N. Ekanayake, C. Léveillé, C. Von Korff Schmising, D. Schick, K. Yao, X. Liu, G. S. Chiuzbăian, J. Lüning, B. Vodungbo, and E. Jal, Toward ultrafast magnetic depth profiling using time-resolved x-ray resonant magnetic reflectivity, *Struct. Dyn.* **8**, 034305 (2021).
- [58] B. L. Henke, E. M. Gullikson, and J. C. Davis, X-ray interactions: Photoabsorption, scattering, transmission, and reflection at $E = 50\text{--}30,000$ eV, $Z = 1\text{--}92$, *At. Data Nucl. Data Tables* **54**, 181 (1993).
- [59] J. K. Dewhurst, S. Sharma, L. Nordström, F. Cricchio, O. Grånäs, and H. Gross, The ELK Code (2018), elk.sourceforge.net/.
- [60] S.-G. Gang, R. Adam, M. Plötzing, M. von Witzleben, C. Weier, U. Parlak, D. E. Bürgler, C. M. Schneider, J. Rusz, P. Maldonado, and P. M. Oppeneer, Element-selective investigation of femtosecond spin dynamics in NiPd magnetic alloys using extreme ultraviolet radiation, *Phys. Rev. B* **97**, 064412 (2018).
- [61] B. Watts, Calculation of the Kramers-Kronig transform of x-ray spectra by a piecewise Laurent polynomial method, *Opt. Express* **22**, 23628 (2014).
- [62] M. Battiato, K. Carva, and P. M. Oppeneer, Superdiffusive spin transport as a mechanism of ultrafast demagnetization, *Phys. Rev. Lett.* **105**, 027203 (2010).
- [63] B. Koopmans, M. van Kampen, and W. J. M. de Jonge, Experimental access to femtosecond spin dynamics, *J. Phys.: Condens. Matter* **15**, S723 (2003).
- [64] C. Möller, H. Probst, G. S. M. Jansen, M. Schumacher, M. Brede, J. K. Dewhurst, M. Reutzler, D. Steil, S. Sharma, and S. Mathias, Verification of ultrafast spin transfer effects in FeNi alloys, [arXiv:2306.02793](https://arxiv.org/abs/2306.02793).
- [65] H. Probst, C. Möller, M. Schumacher, T. Brede, J. K. Dewhurst, M. Reutzler, D. Steil, G. S. M. Jansen, S. Sharma, and S. Mathias, Replication data for: Unraveling femtosecond spin and charge dynamics with EUV T-MOKE spectroscopy (2023), <https://doi.org/10.25625/CDBY3D>.
- [66] K. Krieger, P. Elliott, T. Müller, N. Singh, J. K. Dewhurst, E. K. Gross, and S. Sharma, Ultrafast demagnetization in bulk versus thin films: An *ab initio* study, *J. Phys.: Condens. Matter* **29**, 224001 (2017).
- [67] J. K. Dewhurst, K. Krieger, S. Sharma, and E. K. Gross, An efficient algorithm for time propagation as applied to linearized augmented plane wave method, *Comput. Phys. Commun.* **209**, 92 (2016).